Journal of Nuclear Materials 627 (2026) 156607

Contents lists available at ScienceDirect

Journal of Nuclear Materials

journal homepage: www.elsevier.com/locate/jnucmat

Improving the corrosion resistance of structural materials in liquid lead-bismuth eutectic alloys: Combined machine learning and molecular dynamics

Weihan Li [a], Wenrui Wang [a,*], Qing Peng [b], Lu Xie [a,*]

[a] School of Mechanical Engineering, University of Science and Technology Beijing, Beijing 100083, China
[b] School of Power and Mechanical Engineering, Wuhan University, Wuhan 430072, China

HIGHLIGHTS

- A process combining machine learning and MD simulation for material property prediction.
- The optimized HEAs exhibit enhanced corrosion resistance against liquid LBE alloy.
- MD simulation of HEAs dissolution corrosion in liquid LBE environment.

ARTICLE INFO

Keywords:
Machine learning
Molecular dynamics
Alloy composition optimization
Dissolution corrosion
LBE alloy

ABSTRACT

The dissolution–corrosion behavior of structural materials in liquid lead–bismuth eutectic (LBE) was investigated at the atomic scale. Given the nanometer and sub-nanosecond scales of molecular dynamics, the penetration and dissolution metrics are used for comparative screening rather than direct prediction of long-term corrosion rates or reactor lifetimes. An integrated machine learning–molecular dynamics (ML–MD) workflow was developed to optimize the composition of Co–Cr–Fe–Ni–Al–Mo–Ti multi-component alloys across 3–400 million virtual candidates. Under identical MD conditions, corrosion resistance was assessed via LBE penetration depth and dissolution degree, with the optimized composition predicted to exhibit a penetration depth approximately one-eighth that of nuclear-grade FeCrAl. The composition window was broadened to facilitate mechanistic interrogation and ML dataset construction; given Co content restrictions in nuclear materials, the predicted compositions represent screening outcomes rather than deployment recommendations. Furthermore, supplementary Co-free simulations, guided by ML-derived element importance ranking, demonstrate improved corrosion resistance over FeCrAl yet fall short of the Co-containing optimized composition, confirming Co's significant contribution to LBE corrosion resistance and indicating that a trade-off between corrosion performance and activation compliance warrants further investigation in Co-restricted nuclear applications. Overall, this work provides an efficient computational framework for rapid discovery and optimization of multi-component alloys with enhanced LBE corrosion resistance, offering a promising strategy to guide materials development for advanced nuclear reactor systems.

1. Introduction

The liquid lead-bismuth eutectic (LBE) alloys serve as the coolant for the fourth-generation lead-cooled fast reactors, which ensures safe operation of the reactors [1–3]. However, under the necessary conditions for the reactor to work, the high temperature (the melting point of LBE is around 396.7 K-398.7 K), flow rate, and density of the liquid LBE can cause damage to the materials of the reactor due to oxidative and dissolution corrosion [4–7]. In the case of oxidative corrosion, the surface of the alloy reacts with oxygen to form an oxide layer. Dissolution corrosion involves the dissolution of structural materials in liquid LBE alloys, resulting in degradation of alloy properties and material loss. It should be noted that the dissolution of structural materials not only affects the properties of the substrate but also impacts the formation of

* Corresponding authors.
E-mail addresses: gmbitwrw@ustb.edu.cn (W. Wang), xielu@ustb.edu.cn (L. Xie).

https://doi.org/10.1016/j.jnucmat.2026.156607
Received 23 July 2025; Received in revised form 19 March 2026; Accepted 19 March 2026
Available online 20 March 2026

the surface oxide film. In the early stages of oxide film formation, the dissolution process may have a significant influence on structure and stability. As the structural materials dissolve, the dissolved elements react with the available oxygen, which can lead to changes in the composition and structure of the oxide film. Moreover, the metal ions released can form new metal-oxide interfaces, further affecting the structure and stability of the oxide film [8]. Consequently, it is crucial to reduce the degree of dissolution of structural materials in liquid LBE to ensure the structural integrity of the surface and to achieve a high degree of corrosion resistance. Nevertheless, qualification of structural materials for LBE-cooled reactors requires multiple criteria beyond corrosion resistance, including high-temperature mechanical performance, creep/fatigue behavior, and irradiation tolerance. In this work, we focus on dissolution-driven degradation as an initial screening criterion at the atomic scale.

In recent years, significant research effort has focused on developing corrosion-resistant materials for applications with liquid LBE alloy. Zhang et al. [9] investigated the effect of trace Si addition on FeCrAl coatings' liquid LBE corrosion resistance. The results demonstrated that Si doping promotes the formation of a protective Al_2O_3-rich oxide layer and creates a Si diffusion barrier, significantly enhancing the coating's corrosion resistance in lead-bismuth eutectic environments. Ma et al. [10] summarized the current state of the development of FeCrAl alloys as potentially important structural materials in accelerator-driven subcritical (ADS) and lead-cooled fast reactor (LFR) systems and considered corrosion experiments with high-temperature liquid LBE/Pb alloys. It was found that corrosion resistance can be improved by controlling the alloy composition, adding reactive elements, and controlling the oxygen concentration. In the development of structural materials resistant to liquid LBE corrosion, more attention has been paid to the roles of various component elements. However, traditional alloys are limited in terms of variation and associated performance due to the restrictions on the number of main elements. Furthermore, given the harsh and rigorous environment in nuclear reactors, it is increasingly challenging for traditional alloys to meet the performance requirements of structural materials in service. Multi-component high-entropy alloys (HEAs) offer a greater material design space and a consequent greater scope in terms of performance [11].

In the exploration of the corrosion resistance of multi-element HEAs to liquid LBE, Gong et al. [12] examined the tensile mechanical properties of two Al_xCoCrFeNi alloys ($x = 0.3$ and $x = 0.4$) in liquid LBE at temperatures of 623 K and 773 K. It was found that LBE causes only mild overall degradation in the tensile properties of $Al_{0.3}$CoCrFeNi; however, embrittlement signatures were still observed, including cleavage at 623 K and a tendency for intergranular cracking at 773 K. In contrast, $Al_{0.4}$CoCrFeNi shows weak degradation at 623 K but severe deterioration at 773 K. Deng et al. [13] designed and prepared a refractory TiNbZrMoV multi-component alloy coating using the magnetron sputtering technique and conducted saturated oxygen static corrosion tests on liquid LBE to investigate the corrosion behavior of the coatings at 923 K. It was found that the coatings maintained excellent integrity and significantly mitigated the corrosion of ferritic/martensitic steels by liquid LBE. This effect is attributed to the inherent low solubility of the constituent elements in the coating, which limits the diffusion or segregation of the elements from the steel and the coating. Although some progress has been made in the development of multi-component alloys in nuclear environments, the large number of primary elements poses a serious challenge to compositional control. The corrosion of structural materials in liquid LBE results from the interaction of Pb and Bi atoms with the surface of structural materials. These processes typically occur at small time and length scales, which are difficult to capture in experimental tests. As a direct consequence, the development of structural materials resistant to liquid LBE corrosion faces ongoing challenges.

Molecular dynamics (MD) simulations play a crucial role in microscale materials research and have been widely used for studying material properties and testing material performance [14–16]. Xiong et al. [17] investigated the application of microscale simulations in the study of dissolution and oxidation corrosion mechanisms involving steel and liquid LBE, explored the effects of stress and grain boundaries and the utilization of surface coating and corrosion inhibitors, and provided a guide to related experiments. Moreover, MD simulation methods have been used to investigate the mechanism of material corrosion and penetration features at an atomic scale. Maulana et al. [18] investigated the corrosion of steel in liquid lead-cooled reactors using MD simulations. At 773 K, the diffusion depths of Pb atoms in $FeNi_{10}Cr_{16}$, $FeNi_{10}$, and $FeCr_{16}$ are 1.18 Å, 7.25 Å, and 11.08 Å, respectively. Gao et al. [19, 20] applied the embedded-atom method (EAM) within the MD framework to simulate the physical properties of liquid lead, bismuth, and the binary LBE alloy. By comparing the simulation results with the experimental results, it was found that the densities and thermal expansion coefficients were in good agreement, demonstrating the effectiveness of the MD simulation method in exploring the physical properties of liquid metal alloys. Zhou et al. [21] investigated the solid-liquid interface between BCC-Fe (100) and liquid LBE under anaerobic conditions using classical MD simulations and EAM. Both static and dynamic simulations indicated that Fe atoms preferentially bind with Bi rather than Pb. The MD simulation enables a detailed assessment of material dissolution in liquid LBE and permeation into the material matrix, especially when combined with radial distribution function (RDF) and mean square displacement (MSD) analysis [22–25].

Although MD simulations can provide insight into the dissolution of specific components of structural material in liquid LBE to provide a reference for material design, the overall process relies on trial and error. Moreover, this approach requires significant computational costs, and it is difficult to accurately predict the composition of the material. The advent of machine learning (ML) methods has effectively addressed this issue. By learning from existing data features and employing black-box modeling, it is possible to predict the composition of materials with specific properties [26,27]. Currently, ML methods have made significant achievements in the field of materials science and have become an increasingly active research topic, providing solutions for complex materials design [28]. Halpren et al. [29] combined ML with first principles to discover eight new hydrogen storage multi-component alloys. Klimenko et al. [30] developed data-driven machine learning models, identifying the support vector classifier as optimal for predicting ductility in high-entropy alloys (balanced accuracy: 0.784), and integrated it with strength models to design novel Al-Cr-Nb-Ti-V-Zr HEAs, with $Al_1Cr_9Nb_{35}Ti_5V_{40}Zr_{10}$ exhibiting high strength and ductility, overcoming traditional strength-ductility trade-offs. Chen et al. [31] combined ML and MD simulation methods and set out to optimize yield strength as a target material property using valence electron concentration and vacancy formation energy as input features. $V_5Cr_{16}Fe_{9.}Co_{35}Ni_{35}$ was successfully identified as the alloy with the highest yield strength in the search space, with Co-Cr-Fe-Ni as the main component and vanadium as the secondary component. Shen et al. [32] used seven ML classification models to analyze and predict the phase structure of multi-component alloys. Using root mean square error (RMSE) and mean absolute error (MAE) as evaluation metrics, the results demonstrated that the extreme gradient boosting (XGB) model performs the best in terms of classification and regression predictions.

A comprehensive review of the literature reveals that molecular dynamics simulations serve as a fundamental tool for investigating the corrosion resistance mechanisms of structural materials in liquid lead-bismuth eutectic environments at atomic scales, while machine learning methods facilitate rapid composition-property predictions through data-driven modeling. MD simulations offer distinct advantages for preliminary material screening and composition optimization, particularly in terms of computational efficiency, cost-effectiveness, and safety considerations when handling hazardous liquid metal systems. The method enables direct observation of atomic-scale dissolution behaviors and interfacial interactions that are experimentally inaccessible,

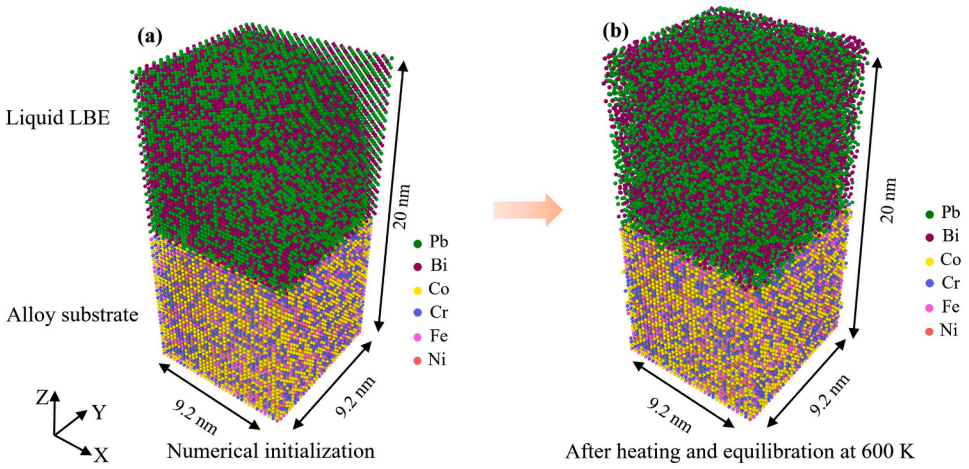

Fig. 1. Atomistic model of multi-component alloys in contact with liquid lead–bismuth eutectic LBE. CoCrFeNi is shown only as a representative example, and other multi-component alloys were generated from the same base geometry by assigning chemical species to the substrate lattice sites to match the target compositions. The alloy substrate is constructed on a body-centered-cubic BCC lattice template: (a) Initial configuration: Pb and Bi atoms are numerically initialized on a face-centered-cubic FCC lattice to create a uniform and dense starting packing above the substrate; (b) Configuration after heating and equilibration at 600 K, which is above the Pb–Bi eutectic melting temperature of about 398 K: the LBE becomes fully molten and structurally disordered.

allowing systematic exploration of compositional effects on corrosion resistance across a wide range of alloy chemistries. For the nuclear energy community, this integrated ML-MD framework offers a practical screening tool that can significantly reduce the time and cost associated with developing LBE-resistant materials. By identifying promising compositions computationally, experimental efforts can focus on validating a limited number of pre-screened candidates rather than exploring the vast compositional space through trial-and-error experimentation.

Inherent limitations of MD simulations must be acknowledged. The nanometer length scale and sub-nanosecond time scale of MD preclude direct prediction of macroscopic corrosion rates observed in engineering applications. The penetration depth and dissolution metrics obtained in this study are employed for comparative screening under identical simulation conditions rather than absolute performance prediction. Several important phenomena are beyond the scope of this computational framework, including oxidation processes and oxide film formation in oxygen-containing LBE environments, as well as liquid metal embrittlement and other degradation modes involving coupled mechanical loading. The present MD simulations focus on the early-stage dissolution-dominated penetration and transient dissolution/diffusion of matrix elements in oxygen-free LBE prior to appreciable oxide formation. This combined computational approach enables accelerated materials discovery by bridging fundamental mechanism understanding with high-throughput performance prediction.

In this context, we develop an ML-MD framework to identify liquid lead-bismuth eutectic resistant material compositions. The MD simulations provide atomic-scale insights into dissolution behaviors of structural materials in LBE environments and generate fundamental corrosion data. Machine learning algorithms then process these MD datasets to extract composition-performance relationships and establish predictive models. Using this ML predictive capability, we screen large material design spaces to identify optimal compositions with high resistance to LBE dissolution corrosion. Given Co content restrictions in nuclear materials, supplementary simulations of Co-free compositions designed based on the ML-derived element importance ranking are further performed. This combined methodology offers an efficient pathway for developing low-solubility structural materials and advances materials innovation for fourth-generation lead-cooled fast reactor applications.

2. MD-based data sample construction

The machine learning (ML) dataset was generated from molecular dynamics (MD) simulations conducted using the LAMMPS software package [33]. The structural materials performance space comprised alloys with elemental compositions of Co, Cr, Fe, Ni, Al, Mo, and Ti, while the liquid lead-bismuth eutectic (LBE) alloy consisted of Pb and Bi. No oxygen species were included and oxidation/oxide-layer formation was not modeled; thus, the simulations isolate dissolution- and penetration-driven degradation in oxygen-free Pb–Bi (LBE). The simulation model, depicted in Fig. 1, illustrates the interaction between a crystalline alloy substrate and liquid LBE, with CoCrFeNi shown as a representative example. The simulation box dimensions were 9.2 nm × 9.2 nm × 20 nm, with Pb and Bi atoms positioned in the upper region and structural material atoms in the lower region. The CoCrFeNi substrate included 65,536 atoms (16,384 atoms per element: Co, Cr, Fe, Ni), while the LBE system comprised 104,102 Pb atoms and 127,234 Bi atoms, maintaining the eutectic atomic ratio of 44.5 at.% Pb and 55.5 at.% Bi, consistent with nuclear-grade LBE coolant. This configuration ensured chemical fidelity to operational liquid metal environments, enabling accurate assessment of alloy corrosion resistance for compositional optimization. To generate a uniform and dense starting configuration for LBE, Pb and Bi atoms were initially arranged on an FCC lattice as a numerical initialization. The system was then heated to 600 K and equilibrated. Since 600 K is well above the eutectic melting temperature of Pb–Bi LBE, about 398 K, the LBE becomes a fully molten disordered liquid.

The choice of interatomic potentials is pivotal in molecular dynamics simulations, significantly affecting the accuracy of computational outcomes. Material-specific potential parametrization is meticulously applied, with the embedded-atom method (EAM) preferred for metallic systems due to its established effectiveness in capturing metallic bonding characteristics [34]. Under the EAM formalism, the total energy of a metallic system is expressed as a function of pairwise interactions and embedding energies, providing a robust framework for modeling alloy behavior in corrosion studies involving liquid lead-bismuth eutectic (LBE). The total energy of the metallic system under EAM formalism can be expressed as:

$$E = \sum_i F_i(\rho_i) + \frac{1}{2}\sum_t \sum_{i \neq j} \phi_{ij}(r_{ij}) \quad (1)$$

where: r_{ij} is the distance between atom i and atom j, $\varphi_{ij}$is the pair energy

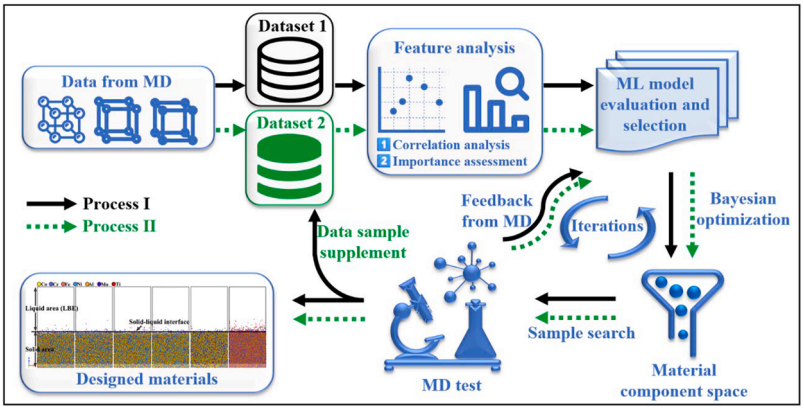

Fig. 2. Optimization to achieve structural material resistance to liquid LBE dissolution corrosion. Process I is completed based on the target of LBE penetration depth. Process II is completed based on the target of structural material degree of dissolution.

between of r_{ij}, $F_i$is the embedding energy of embedding of atom i in a region with an electron density of ρ_i, and ρ_i is the primary electron density.

ρ_i is the sum of the electron cloud densities produced by all the extranuclear electrons in the system except for the i_{th} atom, which can be expressed as:

$$\rho_i = \sum_{i(i\neq j)} \rho_i^{\alpha}(r_{ij}) \tag{2}$$

where $\rho_i^{\alpha}(r_{ij})$ is the electron density distribution function for atom i.

Building on our prior work [35–37], we extend the same EAM-based framework to Co–Ni–Mo–Ti and Pb–Bi cross interactions by systematically scaling the potential parameters reported by Zhou et al. and Gao et al. using a dimensionless scaling factor μ [19,21]. This procedure follows the invariance property of the EAM formalism, in which a consistent rescaling of the elemental electron density functions and the corresponding embedding function preserves the total potential energy and maintains internal consistency of the parameter set. Specifically, we keep the Pb and Bi parameters unchanged as the reference standard and rescale the elemental electron density functions of the additional alloying elements by μ. At the same time, the embedding function is redefined consistently so that the total energy calculated under EAM remains invariant, as expressed in Eq. (3):

$$F_i'(\eta) = F_i(\eta/\mu) = F_i[(\mu \times \rho_i)/\mu] \tag{3}$$

The choice of individual electron densities is arbitrary. We modified the density functions ρ_i^{α} of each element, while keeping the parameters for Pb and Bi unchanged, to ensure the same density standard for both:

$$\rho_i^{\alpha'}(R) = \mu \times \rho_i^{\alpha}(R) \cdot F_i'(\eta) = F_i(\eta/\mu) \tag{4}$$

where i represents the elements Co, Mo, or Ti. In this work, μ is set to 0.0097, adopting the value reported by Gao et al. for diffusion simulations of Fe and Ni in liquid LBE based on molecular dynamics and first-principles-supported validation [20]. Following the same rationale, the selected μ enables matching of the Pb electron density at a reference separation R = 3.00 Å between the Zhou parameter set and the Belashchenko parameter set [21,38]. Using a single μ consistently for the same set of matched parameters is essential; otherwise, the intrinsic consistency of the EAM parameterization would be compromised. With this procedure, the parameter matching for each alloying element with Pb and Bi is achieved in a controlled and reproducible manner. This matching strategy is intended to provide a consistent cross-interaction description for comparative screening under the present MD conditions.

To avoid nonphysical start-up artifacts due to excessively short initial interatomic distances at the solid–liquid interface, a 1.5 Å gap was introduced between the liquid LBE and the alloy surface [21,37]. This separation is used only for initialization and is removed naturally during equilibration as the liquid relaxes toward the surface. Four layers of fixed atoms were placed at the top and bottom to eliminate the influence of periodic boundary conditions in the Z-direction. The lattice constant of the structural materials was set to 2.8682 Å, and the solid substrate was constructed on a body-centered-cubic (BCC) lattice template [37]. This BCC template was adopted as a standardized crystalline scaffold for high-throughput comparative screening over an ultra-large candidate space, so that all compositions are evaluated under an identical packing density and surface topology and the resulting penetration/dissolution metrics remain directly comparable. In addition, because the design space includes Al, Ti, and Mo, the occurrence of BCC-leaning or mixed BCC tendencies is not unusual in multicomponent alloys; therefore, using a BCC scaffold provides a reasonable and consistent structural baseline for the present ML–MD ranking, rather than an assertion of phase stability for each individual composition. Molecular dynamics simulations employed a time step of 0.001 ps. The system was initialized at 300 K, heated to 600 K over 500 ps, and equilibrated for 50 ps under the canonical (NVT) ensemble. Subsequently, simulations were performed at a constant temperature of 600 K for 500 ps to model dissolution/penetration processes in oxygen-free LBE, ensuring accurate representation of alloy-liquid lead-bismuth eutectic (LBE) interactions.

3. ML modeling

The dissolution process involves not only the dissolution of alloy components into liquid LBE but also the simultaneous destruction and penetration of the alloy matrix by liquid LBE [39–43]. To optimize dissolution-driven corrosion resistance (i.e., resistance to LBE penetration and element dissolution), these two degradation mechanisms were defined as separate optimization targets. The detailed workflow is illustrated in Fig. 2 and consists of five main processes: data collection, feature analysis, model selection, alloy composition iterative search, MD validation. The structural material data samples in the dataset were generated using MD simulations, followed by data preprocessing to remove outliers. In Process I, all feature inputs are elemental compositions, and the output target is the depth to which the liquid LBE alloy penetrates into the structural material matrix. In Process II, the feature inputs are similar to those in Process I, with the main difference being the addition of the feature representing the depth (Depth) to which the liquid LBE alloy penetrates into the structural material matrix. The output target is the number of atoms dissolved in the liquid LBE. Feature analysis primarily uses Pearson correlation analysis and random forest importance algorithms to assess the correlation and importance of features. Pearson correlation analysis is used to measure the linear correlation between any two input features, while the random forest algorithm calculates the relative importance of each feature to the target

attribute. Features are ranked by importance, enabling the determination of the extent to which each element influences the target material performance.

Sample composition screening adopts Bayesian optimization principles, using the Efficient Global Optimization (EGO) algorithm to construct the maximum expected improvement (*EI*) value of the material performance target label in the search space, serving as an indicator for multi-component alloy sample screening. The bootstrapping method is used to resample each material sample in the candidate set, predict its performance, calculate the *EI* value for each alloy sample, and select the top 5 alloy samples with the highest *EI* values in the sample performance space as the screening results for this round of alloy samples.

To improve the accuracy of material composition prediction, 8 ML models were selected and their accuracy was evaluated. For Process I, eight rounds of iterative searches were conducted in the sample space. In each round, the five material composition samples with the highest *EI* values were selected as the search results for that round, and these five material composition samples were fed back into the original dataset to improve and optimize model performance, followed by the next round of searches. Similar to Process I, Process II conducted six rounds of iterative searches in the sample space. Ultimately, alloy samples were obtained through the two ML search pathways. For the alloy samples obtained through the search (five samples from each search pathway), MD simulations of the dissolution corrosion process were conducted from two aspects: the dissolution of the structural material alloy surface and the extent to which the liquid LBE alloy penetrates the surface of the structural material alloy matrix. These results were then compared and analyzed with FeCrAl alloys.

3.1. ML original data collection

In Process I, the optimization target is the penetration depth of Pb and Bi atoms into the structural alloy, which serves as a measure of the material's resistance to LBE infiltration. The input features used in this process are entirely limited to the elemental content of the alloy—i.e., the relative proportions of constituent elements such as Co, Cr, Fe, Ni, Al, Mo, and Ti. The initial dataset includes 251 alloy samples, spanning 47 four-component, 86 five-component, 80 six-component, and 38 seven-component compositions. Detailed original dataset for Process I in supplementary material S1. The output is a set of alloy candidates predicted to have lower penetration depth. These candidates are then validated via MD simulations, and the newly validated data are incorporated into the dataset for the next iteration. Process I proceeds through eight such iterative rounds.

In Process II, the focus shifts to minimizing the number of dissolved atoms, representing the alloy's resistance to component dissolution in liquid LBE. The input dataset is expanded to 279 samples by adding the compositions evaluated in Process I and introducing an additional descriptor: the simulated penetration depth from Process I. Detailed original dataset for Process II in supplementary material S2. The updated feature set, now including both elemental composition and penetration depth, is used to train a new model. Similar to Process I, alloy candidates with improved dissolution resistance are identified and validated through MD simulations, with the data fed back into the model iteratively.

3.2. Material component space design

Based on the structural characteristics of the original dataset, the performance space for the multi-component alloys was set as $Co_xCr_yFe_zNi_uAl_vMo_wTi_n$, where x, y, z, u, v, w, and n represent the atomic percentage of each element, and $x+y+z+u+v+w+n=100$ (at.%). In Process I, a search step size of 1 at.% was set. The search ranges for each element were as follows: $x=0$ or $5<x<30$, $y=0$ or $5<y<20$, $z=0$ or $18<z<49$, $u=0$ or $2<u<16$, $v=0$ or $1<v<29$, $w=0$ or $1<w<4$, and $n=0$ or $1<n<4$. This range is related to the coverage of elements in the original dataset. The material performance space comprised a total of 3105,128 samples, with 4845 samples of four-component alloys, 176,223 samples of five-component alloys, 916,112 samples of six-component alloys, and 2007,948 samples of seven-component alloys.

In Process II, the search range for each element was defined as follows: $x=0$ or $5<x<30$, $y=0$ or $5<y<20$, $z=0$ or $10<z<49$, $0\le u<21$, $0\le v<29$, $0\le w<4$, and $0\le n<4$. During the first three rounds of iterative searching, the search step size for the main elements (Co, Cr, Fe, Ni, and Al) was set to 1 at.%, whereas the search step size for Mo and Ti was set to 0.5 at.%. The material performance space comprised a total of 10,762,421 alloy samples, including 5550 samples with four-component alloys, 251,885 samples with five-component alloys, 1629,332 samples with six-component alloys, and 8875,654 samples with seven-component alloys. In the fourth to sixth rounds of searching, the search step sizes for elements were further refined, and the search space samples expanded to approximately 400 million. It should be noted that, in both Process I and Process II, the elemental ranges were deliberately selected to ensure sufficient compositional diversity for mechanistic investigation and for training/interpretation of the ML models within the present MD–ML framework. Therefore, the resulting compositional space should be regarded as a model system for trend learning rather than a set of candidate alloys intended for nuclear deployment; for nuclear-oriented material development, the present workflow can be straightforwardly coupled with additional engineering constraints to guide practical down-selection and experimental validation.

During the sample search process, the Bayesian optimization (BO) method was employed to strategically explore the high-dimensional composition space of multicomponent alloys and fully leverage its sample efficiency advantages in resource-constrained optimization scenarios [44,45]. By assuming a Gaussian process (GP) surrogate model to approximate the probabilistic distribution of target performance predictions, the Efficient Global Optimization (EGO) algorithm constructs an acquisition function termed expected improvement (*EI*), which represents the current best performance [46]. This framework explicitly balances exploration of uncertain regions and exploitation of high-performance candidates, enabling systematic prioritization of alloy compositions with maximal potential performance gains while minimizing molecular dynamics (MD) simulations or experiments. The dissolution process involves not only the dissolution of alloy components into liquid LBE but also the simultaneous destruction and penetration of the alloy matrix by liquid LBE; therefore, the optimization objectives include two key performance indicators: reducing the number of dissolved matrix atoms and lowering the penetration depth of LBE in the alloy matrix. The expression for *EI* is as follows:

$$EI = E[\max(\mu^* - y, 0)] = \int_{\mu^*}^{\infty} (\mu^* - y) P(y|x') dy = \sigma[\varphi(z) + z\phi(z)] \tag{5}$$

$$z = \frac{(\mu^* - \mu)}{\sigma} \tag{6}$$

where y represents the mean predicted target performance, μ^* denotes the optimal value of the target performance in the dataset (in this study, the optimal value is the minimum number of dissolved atoms in the matrix and the lowest liquid LBE penetration depth), $P(y|x')$ is the distribution of predicted values for each sample in the search space, μ represents the mean of predicted values for each sample in the search space, and σ is the standard deviation of predicted values. In addition, $\mu^* - y$ represents the potential improvement in performance for the alloy samples, $\varphi(z)$ denotes the standard normal distribution of predicted target values, and $\phi(z)$ is the cumulative distribution function of predicted target values for alloy material performance.

The bootstrapping method was employed to predict the performance of each material sample within the candidate set. This resampling

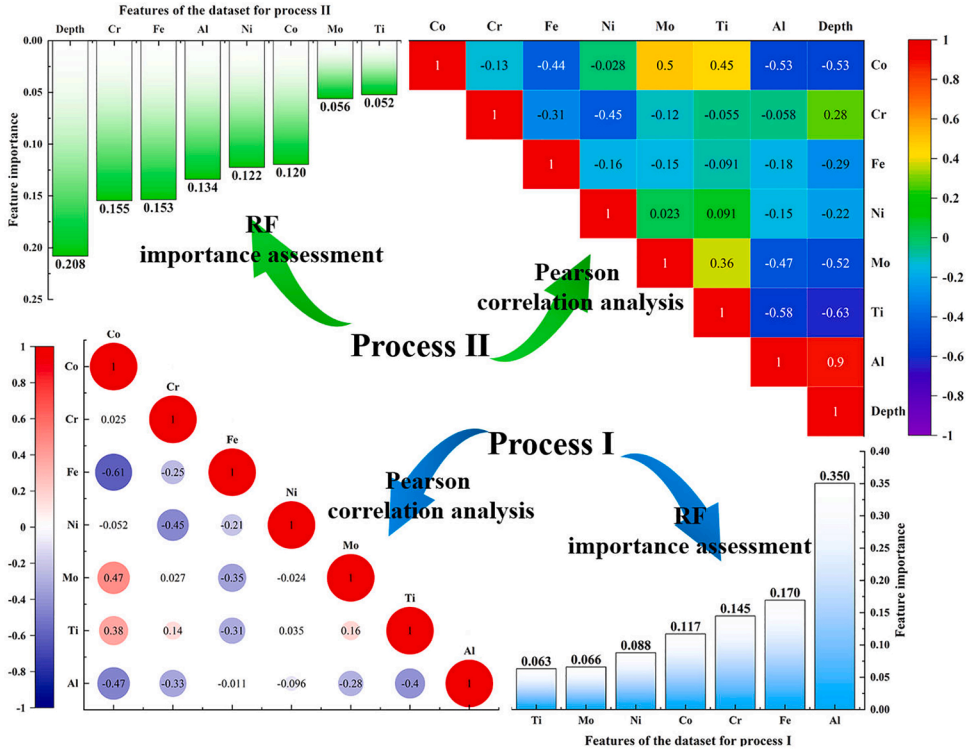

Fig. 3. Pearson correlation analysis and random forest importance evaluation of the dataset feature attributes.

technique quantifies statistical uncertainties by generating multiple surrogate datasets through random sampling with replacement from the original experimental observations [47]. This approach addresses model overfitting risks inherent in small materials datasets while quantifying prediction confidence intervals. Specifically, 1000 resampled datasets matching the initial dataset size were created, each used to train independent machine learning (ML) models. During each iteration of sample selection, all candidate alloys received 1000 parallel predictions from these bootstrapped ML models. The ensemble outputs provided mean predicted performance values (μ) and uncertainty estimates (σ) through their standard deviations—critical parameters for calculating the expected improvement (*EI*) acquisition function (Eq. (5)). The top five alloys with maximal *EI* values were prioritized for subsequent molecular dynamics (MD) simulations.

3.3. ML feature analysis

Pearson correlation analysis and permutation-based random forest (RF) importance assessments were performed on the feature sets of the Process I and Process II datasets, as shown in Fig. 3. Pearson correlation analysis quantifies linear relationships between variables, whereas RF permutation importance estimates each feature's contribution to the target variable by randomly permuting its values in the out-of-bag (OOB) samples and measuring the resulting increase in prediction error [48]. For detailed information, please refer to supplementary materials S3 and S4. The Process I dataset contains seven features corresponding to the elemental compositions of Co, Cr, Fe, Ni, Al, Mo, and Ti, while the Process II dataset extends this set by introducing an additional "Depth" feature, which represents the penetration depth of liquid lead–bismuth eutectic (LBE) into the structural material matrix.

For Process I, Pearson correlation analysis revealed no strong correlations among the elemental features (absolute Pearson correlation values < 0.9), indicating the absence of pronounced interdependence among the elemental compositions with respect to their contributions to material performance. The RF permutation importance assessment ranked the features as Al > Fe > Cr > Co > Ni > Mo > Ti, indicating that the Al content has the largest influence on the depth of liquid LBE penetration into the matrix. For Process II, the "Depth" feature showed the strongest correlation with the Al content, with a Pearson correlation coefficient of 0.9, consistent with the Process I result that identifies Al as the most influential feature governing liquid LBE penetration. The RF permutation importance ranking for Process II was Depth > Cr > Fe > Al > Ni > Co > Mo > Ti, showing that the newly introduced "Depth" feature plays a central role in predicting the dissolution behavior of the structural material matrix in liquid LBE. When the "Depth" feature is excluded, Fe, Al, and Cr consistently appear among the top three features in the RF permutation importance rankings for both Process I and Process II, demonstrating their significant influence on the resistance of structural materials to dissolution corrosion by liquid LBE. In contrast, Mo and Ti consistently rank lowest, which is likely attributable to their relatively low concentrations (< 5 at.%) in the alloy compositions, thereby limiting their effect on corrosion resistance.

3.4. ML model evaluation and selection

To construct predictive models for both Process I and Process II, eight machine learning algorithms were investigated [49]: linear regression (lin) [50], polynomial regression (poly) [51], support vector regression with linear kernel (svr.l) [52], polynomial kernel (svr.p) [52], radial basis function kernel (svr.r) [52], regression tree (cart) [53], back-propagation neural network (bpnn) [54], and k-nearest neighbors (knn) [55]. The performance of these models for Process I and Process II is summarized in Figs. 4(a)-(c) and 5(a)-(c), respectively. The root mean square error (RMSE) is used as the evaluation metric for model prediction capability, where a smaller RMSE value indicates higher prediction accuracy, as expressed in Eq. (7):

$$RMSE = \sqrt{\frac{1}{m}\sum_{i=1}^{m}\left(y_i - \hat{y}_i\right)^2} \tag{7}$$

where m is the number of samples, $y_i$is the calculated value of sample i

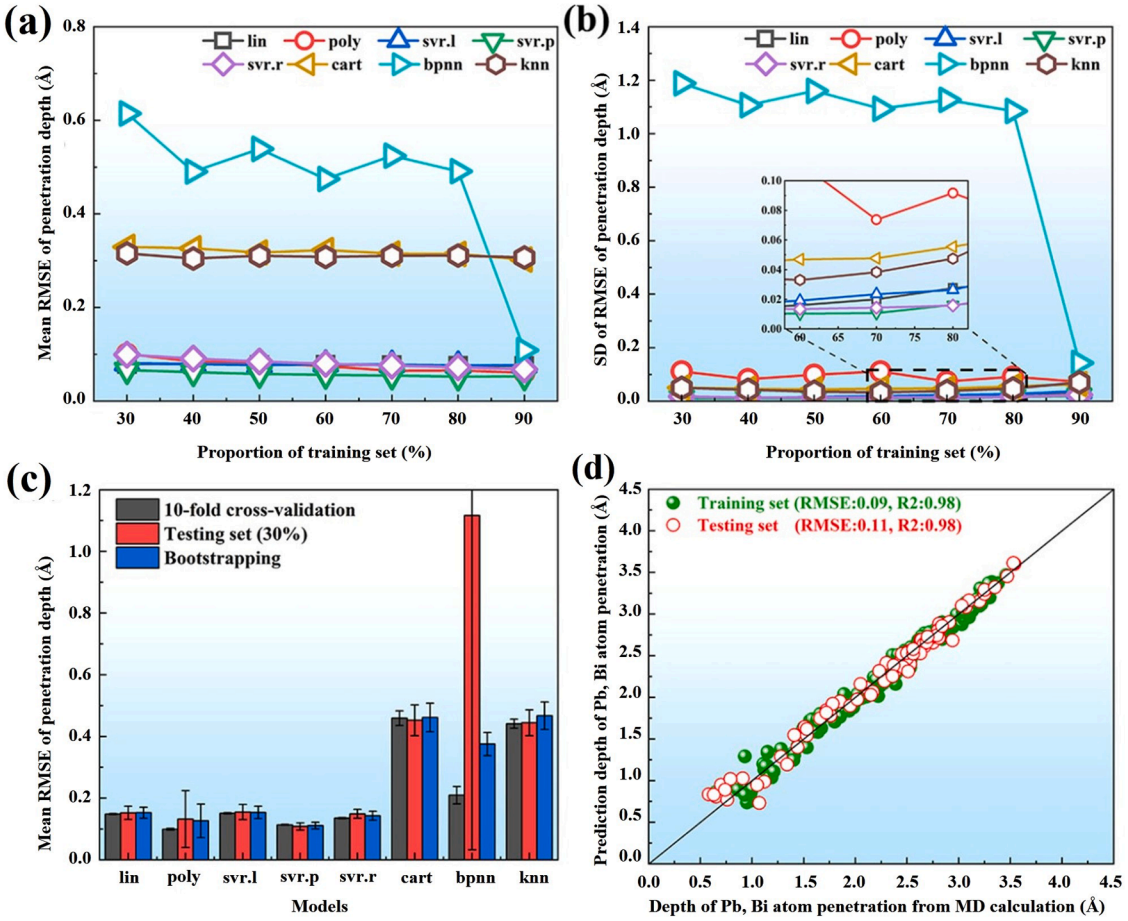

Fig. 4. Model evaluation for Process I using eight machine learning models (lin, poly, svr.l, svr.p, svr.r, cart, bpnn, knn): (a) Mean RMSE of penetration depth over 100 repetitions of the hold-out method at different training–test set ratios; (b) Standard deviation of the 100 RMSE values in (a); (c) Mean RMSE of penetration depth obtained from 100 repetitions of the hold-out method, 10-fold cross-validation, and bootstrapping; (d) Prediction performance of the svr.p model: comparison between ML-predicted and MD-calculated penetration depths.

(MD calculation result), $\hat{y}_i$is the ML predicted value of sample *i*. For Process I, the RMSE has the same unit as the penetration depth (Å), whereas for Process II it has the same unit as the number of dissolved atoms.

For Process I, the root mean square error (RMSE) of the predicted penetration depth is adopted as the primary performance metric. Fig. 4 (a) reports, for each model, the mean RMSE of penetration depth over 100 independent repetitions of the hold-out method at various training–test set ratios, thereby reflecting the prediction accuracy. The corresponding standard deviations (SD) of these 100 RMSE values, which characterize the fluctuation range of the prediction error and thus the stability of each model, are presented in Fig. 4(b). In all cases, the hold-out method [56] is employed, where the dataset is randomly partitioned into training and testing subsets according to predefined ratios, and training-set fractions from 30% to 90% are systematically examined. Because random partitioning introduces sample-to-sample variability, we perform 100 independent modeling and evaluation cycles for each training–test ratio and use the mean RMSE as the final accuracy indicator. As shown in Fig. 4(a), linear regression (lin), polynomial regression (poly), and support vector regression with linear, polynomial, and radial basis function kernels (svr.l, svr.p, and svr.r) all yield relatively low RMSE values, indicating superior predictive accuracy, among which the polynomial kernel model (svr.p) exhibits the best overall performance. Moreover, the RMSE fluctuations of svr.p and svr.r, quantified by the standard deviations in Fig. 4(b), remain small across all training–test ratios, implying excellent prediction stability. When both accuracy and stability are taken into account, svr.p emerges as the most robust model for Process I.

In addition to the hold-out scheme with a 70% training set, 10-fold cross-validation and bootstrapping were employed to further assess the predictive performance of the models, as shown in Fig. 4(c). In the hold-out and cross-validation procedures, a fraction of the data is reserved for testing, thereby reducing the effective training sample size relative to the full dataset, which may influence prediction quality. Bootstrapping mitigates this limitation by drawing samples with replacement so that the training set size remains equal to that of the original dataset, which is particularly advantageous for relatively small datasets. As shown in Fig. 4(c), the polynomial-kernel model svr.p consistently achieves the lowest mean RMSE of penetration depth across the three validation schemes, confirming its superiority over the other models. Fig. 4(d) further illustrates the predictive capability of the svr.p model for Process I, revealing a strong linear correlation between the ML-predicted and MD-calculated penetration depths. The model attains RMSE values of 0.09 Å and 0.11 Å for the training and testing sets, respectively, in quantifying the penetration depth of Pb and Bi atoms into the substrate, and the small discrepancy between these errors indicates robust generalization.

For Process II, an identical model selection procedure was adopted, and the corresponding results are presented in Fig. 5. Fig. 5(a) displays the mean RMSE of dissolved atom number over 100 independent repetitions of the hold-out method for different training–test set ratios. The lin, svr.l, and poly models maintain relatively low RMSE values and show favorable performance across the considered training-set

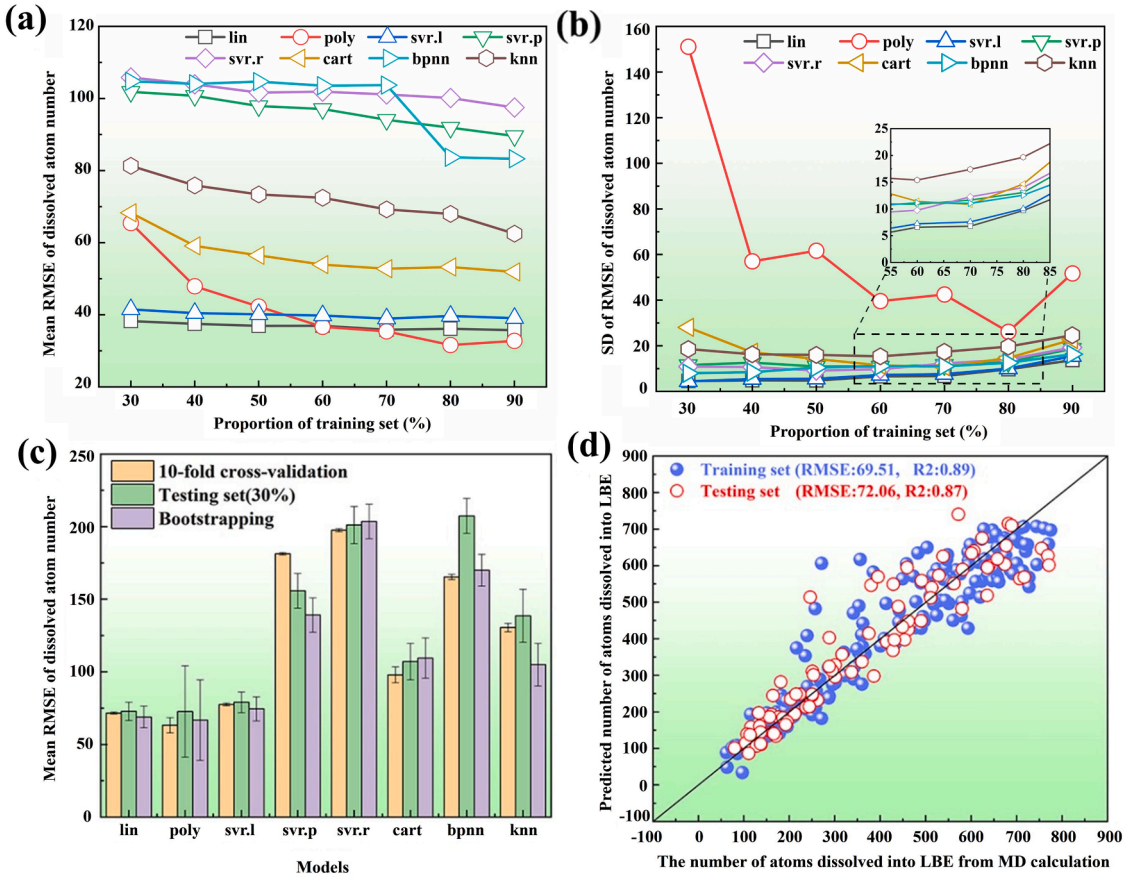

Fig. 5. Model evaluation for Process II using the same eight machine learning models as in Process I. (a) Mean RMSE of dissolved atom number over 100 repetitions of the hold-out method at different training–test set ratios; (b) Standard deviation of the 100 RMSE values in (a); (c) Mean RMSE of dissolved atom number obtained from 100 repetitions of the hold-out method, 10-fold cross-validation, and bootstrapping; (d) Prediction performance of the lin model: comparison between ML-predicted and MD-calculated dissolved atom numbers.

proportions, whereas the remaining models exhibit noticeably higher errors. In addition, the RMSE of all models tends to decrease as the training-set proportion increases, and at a 70% training fraction, the lin and poly models achieve similarly low error levels. Fig. 5(b) reports the standard deviations of the 100 RMSE values for each training–test partition, which characterize the fluctuation range of the prediction error. Among all models, poly exhibits the largest RMSE fluctuations, indicating inferior stability, whereas the other models remain relatively stable for training-set proportions below 70% but show a marked increase in error variability when the training-set fraction exceeds 70%, likely due to the reduced size of the test set leading to less reliable error estimates.

To further examine both the accuracy and stability of the predictions, we also evaluated the models using 10-fold cross-validation and bootstrapping in addition to the hold-out method. Fig. 5(c) summarizes the mean RMSE of dissolved atom number obtained from 100 repetitions of each validation strategy—10-fold cross-validation, the hold-out method, and bootstrapping. Considering both the average RMSE values and their dispersion across the three schemes, the lin model yields the most favorable overall performance for Process II. Fig. 5(d) quantitatively illustrates the predictive capability of the lin model on the Process II dataset, with RMSE values of 69.51 and 72.06 (number of atoms) for the training and testing sets, respectively, and corresponding determination coefficients (R^2) of 0.89 and 0.87. These metrics demonstrate that the lin model can accurately predict the number of dissolved atoms while maintaining strong generalization performance.

4. Results

For Process I, we performed eight iterations of search using the svr.p model. In each iteration, we select the five material component samples with the highest *EI* values as the search results for that round. These samples are validated through MD simulation and fed back into the training data to improve and optimize the model's predictive performance, after which the next round of searches is conducted. Fig. 6(a) presents the penetration depths of Pb and Bi atoms into the alloy matrix across all search iterations, with the optimal candidates from each round highlighted. The alloy sample data points obtained from the search are mainly located in the diagonal area, which indicates the accuracy of the ML method prediction results. Notably, the predicted values consistently fell within the 0–1 Å range, demonstrating the model's effectiveness in identifying alloys with superior resistance to liquid LBE penetration. Fig. 6(b) shows the performance distribution of the original dataset samples and the predicted samples obtained through the search. The 0th iteration represents the original dataset samples, and the optimal sample in the original dataset has a penetration depth of 0.58 Å by the liquid LBE alloy. In the first round of the search, material samples with performance exceeding that of the original dataset were discovered. No material compositions with superior performance were found in the search results of the 2nd to 4th rounds. In the 5th round and subsequent iterations, material samples with performance surpassing that of the original dataset were rediscovered, and samples with even better performance were identified. The top five alloys with the best resistance to liquid LBE alloy penetration among all search results are shown in Table 1.

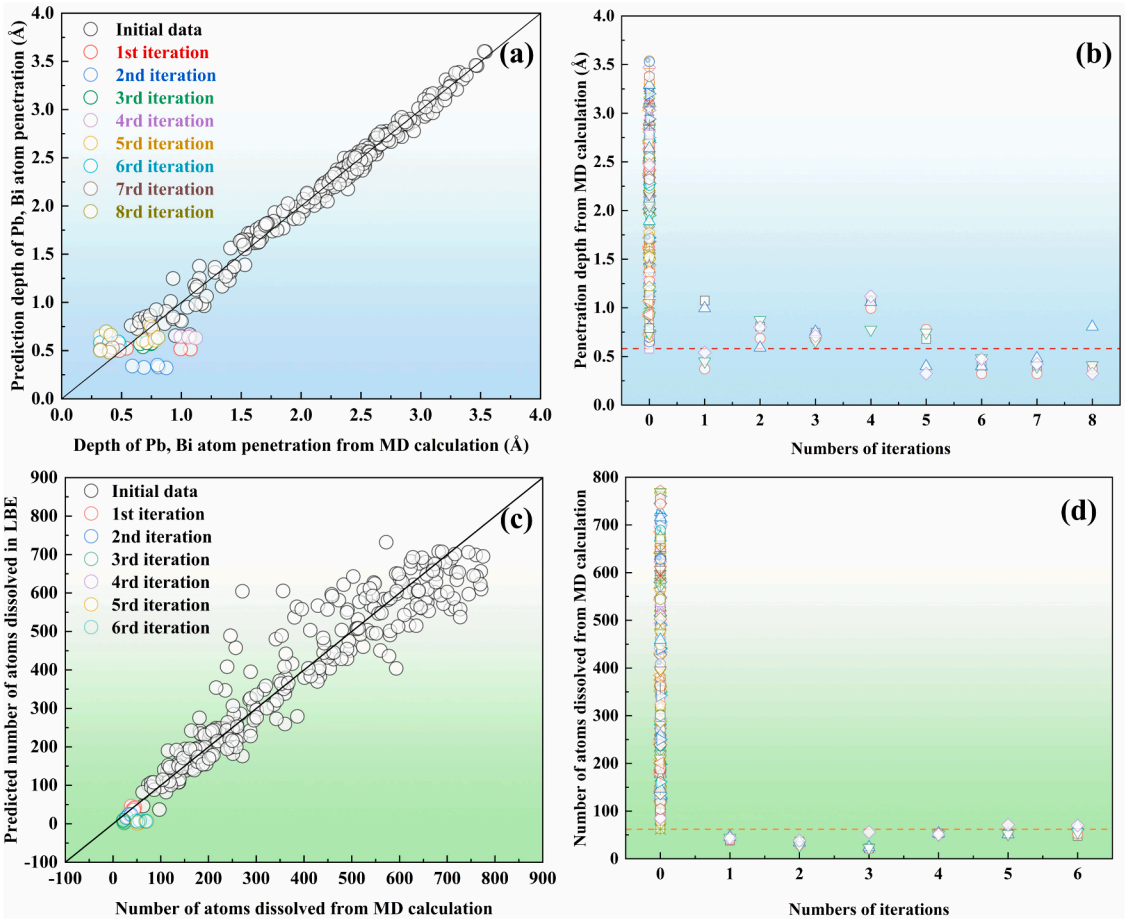

Fig. 6. Diagonal plot of ML prediction results versus MD calculation results and performance comparison between original and predicted samples: (a) and (b) Process I; (c) and (d) Process II.

Table 1
The five alloy components with the best resistance to liquid LBE alloy penetration in the search results in Process I.

No.	Elemental content (at.%)							Penetration depth (Å)
	Co	Cr	Fe	Ni	Al	Mo	Ti	
F8–2	29	5	49	8	1	4	4	0.32
F8–1	29	5	42	15	1	4	4	0.37
F8–3	29	5	41	16	1	4	4	0.40
F7–2	29	6	40	16	1	4	4	0.40
F1–2	28	5	49	9	1	4	4	0.44

Table 2
The five alloy components with the lowest solubility in the search results in Process II.

No.	Elemental content (at.%)							Number of dissolved atoms
	Co	Cr	Fe	Ni	Al	Mo	Ti	
S3–2	25	8	10	28	29	0	0	21
S2–4	28	5	10	20	29	4.5	3.5	22
S3–1	24	8	10	29	29	0	0	24
S3–4	27	8	10	26	29	0	0	26
S3–3	26	8	10	27	29	0	0	28

In Process II, six rounds of search iterations were conducted using a lin model. Similarly, in each iteration, the five material component samples with the highest *EI* values were selected as the results for that round, and the MD calculation values of these five material component samples were fed back into the training data for model optimization, followed by the next round of search. Fig. 6(c) shows the solubility of the matrix material in liquid LBE alloy across all search iterations, with the best candidate materials highlighted in each round. Notably, the samples obtained after six rounds of searching are all located in the initial stage of the diagonal, indicating that the predicted material samples have lower solubility in liquid LBE alloy compared to the original dataset. As shown in Fig. 6(d), samples with lower solubility levels appear in all six rounds of iterative search results, with the most promising candidate sample emerging in the third round of search, demonstrating that the model can effectively identify the optimal material composition. The top five alloys with the lowest solubility among all search results are shown in Table 2. These iterative searches validate the effectiveness of the svr.p and lin models in optimizing alloy compositions to enhance resistance to LBE corrosion.

5. Discussion

5.1. Elemental distribution of search samples

Fig. 7 presents the elemental composition distribution of the identified material samples in the two optimization processes. For Process I, the high-performance samples that appeared in Rounds 5–8 exhibited relatively consistent elemental compositions, as shown in Fig. 7(a). This compositional stability indicates that the search algorithm has converged and found the optimal elemental combination for resisting liquid LBE penetration. As the number of iterations increases, the content of each element tends to stabilize (although Ni and Fe exhibit some fluctuations). The content of Co tends toward the upper limit of the

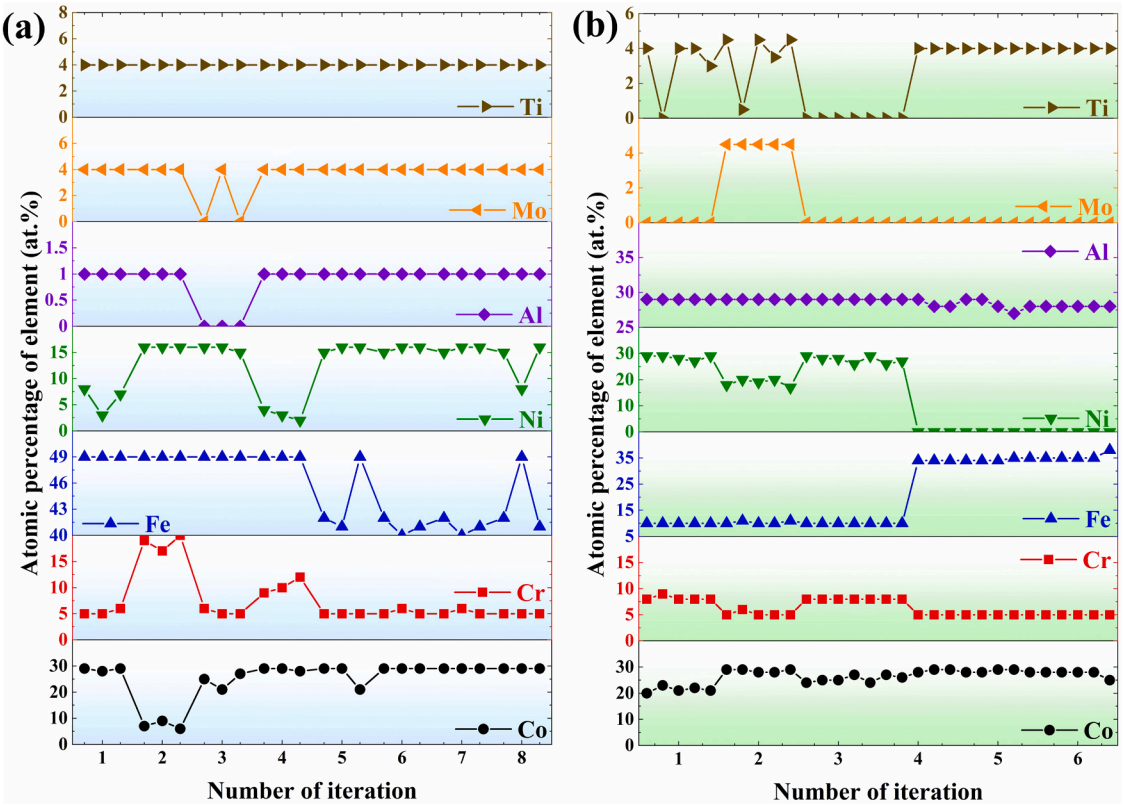

Fig. 7. Elemental content distribution for samples obtained in each round of the search: (a) Process I; (b) Process II.

search range (the upper limit of the Co content range is 30%), while the content of Al tends toward the lower limit of the search range (the lower limit of the Al content range is 0%). Additionally, the Mo and Ti element contents both reached the upper limit of the search range (the upper limit of the Mo and Ti element content range is 4%), which is consistent with the conclusion reported in related studies that adding Mo and Ti elements can enhance the structural material's resistance to LBE corrosion [57].

In Process II, the elemental composition distribution of the material samples obtained through the search is shown in Fig. 7(b). It can be observed that the variation range of elemental compositions in all samples is relatively small, particularly in the top 5 samples with optimal performance. Although there is some variation in the content of trace elements Mo and Ti, it can be observed that the elemental compositions remain at a certain value in consecutive samples, indicating that samples with similar elemental compositions exhibit similar performance. This is even more evident in the variation of the main components Co, Cr, Fe, Ni, and Al. The clear correlation between compositional similarity and performance consistency highlights the accuracy of our material discovery method, proving that alloys within this elemental content range have low solubility in liquid LBE alloys.

5.2. MD validation of search samples

Molecular dynamics simulations were conducted to validate representative alloy samples identified by the two machine-learning search processes. Each candidate and the FeCrAl reference were immersed in liquid LBE for 500 ps under identical simulation conditions. Two metrics were extracted for quantitative comparison: the penetration depth of Pb and Bi atoms into the near-surface region of the substrate and the number of substrate atoms dissolved into the LBE phase. Due to the nanometer length scale and sub-nanosecond time scale accessible to MD, these metrics are used here for comparative screening and ranking under controlled conditions rather than for direct prediction of long-term experimental corrosion behavior. Fig. 8 presents a comparison of the corrosion resistance of the top five alloy samples identified through the search process targeting the penetration depth of liquid LBE alloy with that of FeCrAl alloy after immersion in the liquid LBE alloy for 500 ps. For better visualization, Fig. 8(a) depicts the penetration process of liquid LBE alloy into the substrate, while Fig. 8(b) illustrates the dissolution process of substrate atoms into the liquid LBE alloy.

To further evaluate the corrosion resistance of the alloy samples quantitatively, the penetration depth of Pb and Bi atoms into the substrate surface and the number of dissolved atoms in the liquid LBE alloy were analyzed. It was observed that with increasing immersion time, the penetration depth of the liquid LBE alloy into the substrate exhibited a slight decreasing trend. This behavior can be attributed to the continuous thermal motion of the atoms, where some Pb and Bi atoms that initially penetrated the substrate surface may return to the liquid LBE alloy. Notably, compared to FeCrAl alloys, the alloys obtained through search optimization demonstrated superior performance, as evidenced by the significantly smaller penetration depth of the liquid LBE alloy into the substrate matrix, as shown in Fig. 8(c). Furthermore, the number of dissolved atoms in the liquid LBE alloy was also lower for the optimized alloy samples than for FeCrAl, as shown in Fig. 8(d). Among the candidate alloys, the $Co_{29}Cr_5Fe_{49}Ni_8Al_1Mo_4Ti_4$ alloys exhibited the most promising performance, showing the best resistance to both liquid LBE penetration and material dissolution, indicating improved early-stage resistance under the present MD conditions and supporting its selection as a screening outcome in Process I.

Similarly, Fig. 9 presents a comparison of the corrosion resistance of the top five alloy samples obtained through the search process targeting the dissolution quantity of matrix atoms with that of traditional FeCrAl alloys after 500 ps of immersion in liquid LBE alloy. Fig. 9(a) illustrates the penetration process of the liquid LBE alloy into the matrix, while Fig. 9(b) depicts the dissolution process of matrix atoms in the liquid LBE alloy. Quantitative analysis reveals that the number of atoms dissolved in the liquid LBE alloy for the alloy samples identified through the

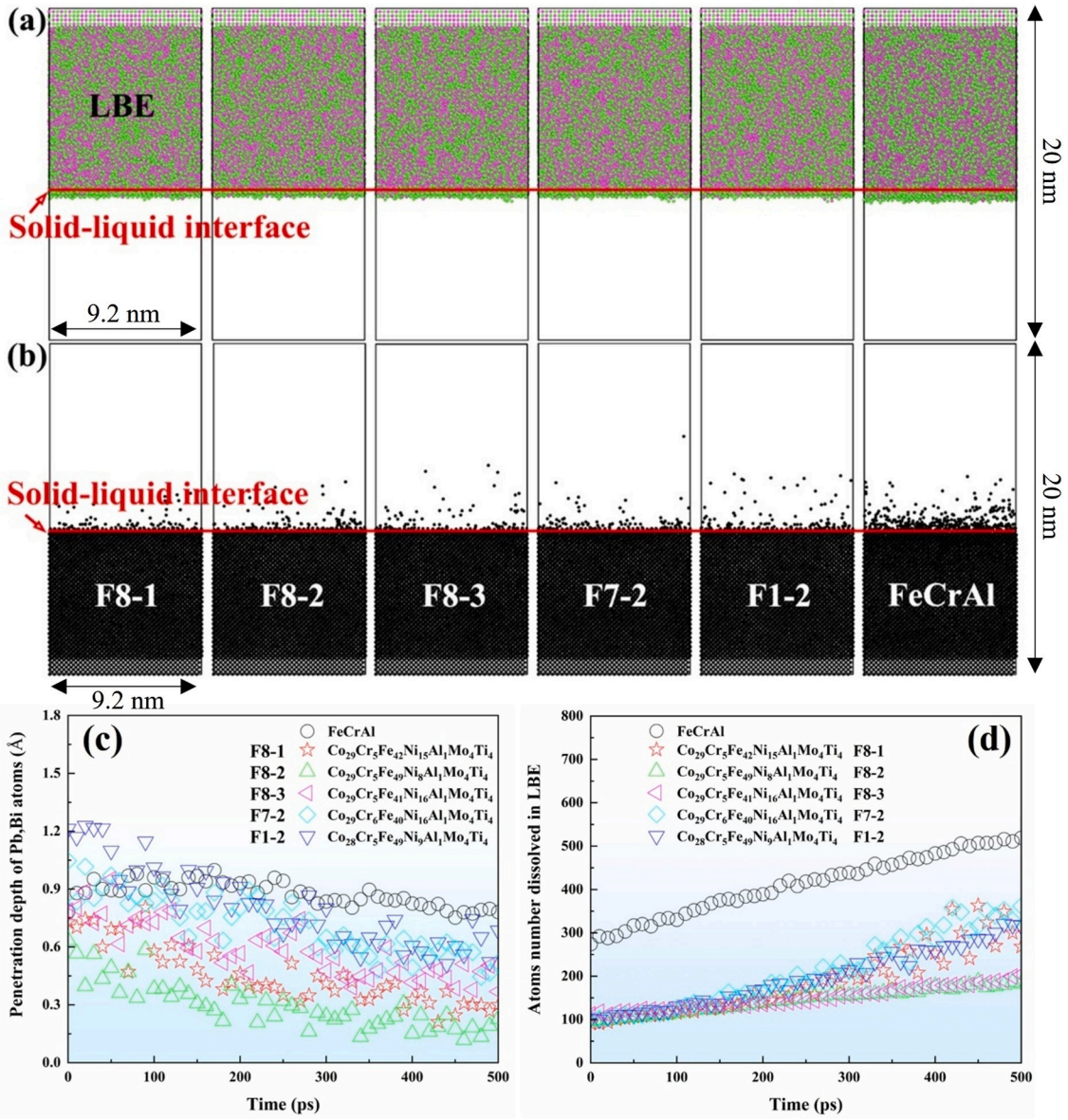

Fig. 8. Performance assessment of material samples obtained from the search in Process I: (a) liquid LBE alloy penetration; (b) matrix atom dissolution; (c) depth of liquid LBE penetration into the matrix; (d) number of matrix atoms dissolved in liquid LBE.

search is significantly smaller than that of the FeCrAl alloy, as shown in Fig. 9(d). Additionally, the number of dissolved atoms increases with prolonged immersion time. Among the candidate alloys, the $Co_{28}Cr_5Fe_{10}Ni_{20}Al_{29}Mo_{4.5}Ti_{3.5}$ composition demonstrates particularly outstanding corrosion resistance. This alloy not only exhibits extremely low dissolution levels in the liquid LBE alloy but also shows excellent resistance to LBE penetration, as evidenced by its shallow penetration depth, as shown in Fig. 9(c). Based on the results of both Process I and Process II, the $Co_{28}Cr_5Fe_{10}Ni_{20}Al_{29}Mo_{4.5}Ti_{3.5}$ alloy was determined to possess the lowest dissolution and the shallowest penetration depth of liquid LBE alloy into the matrix, making it the best-performing screening outcome within the present MD conditions and the explored composition window. The results demonstrate that the ML-guided workflow can efficiently screen and rank alloys using MD-based screening metrics in liquid LBE, thereby providing a computational basis to guide subsequent constrained screening and experimental validation.

5.3. Mechanistic interpretation and considerations for nuclear applications

The optimized alloys identified through the ML-guided search contain approximately 28–29 at.% Co and 4–4.5 at.% Mo. The convergence toward high Co content can be rationalized from the perspective of elemental dissolution thermodynamics. Our previous MD study on CoCrFeNi-based HEAs demonstrated that the diffusion activation energies follow the order Fe < Cr < Ni < Co, indicating that Co atoms exhibit the highest resistance to dissolution among the principal elements [36]. Consequently, increasing Co content effectively reduces the proportion of readily dissolving elements in the alloy matrix, thereby improving overall corrosion resistance. The beneficial effect of Mo addition is also supported by our previous study [36], which showed that Mo retards LBE penetration.

However, practical deployment of these compositions in nuclear systems requires careful consideration of neutron activation constraints. Co-59 undergoes neutron capture to form Co-60, a radioisotope with a half-life of 5.27 years that emits high-energy gamma rays at 1.17 and

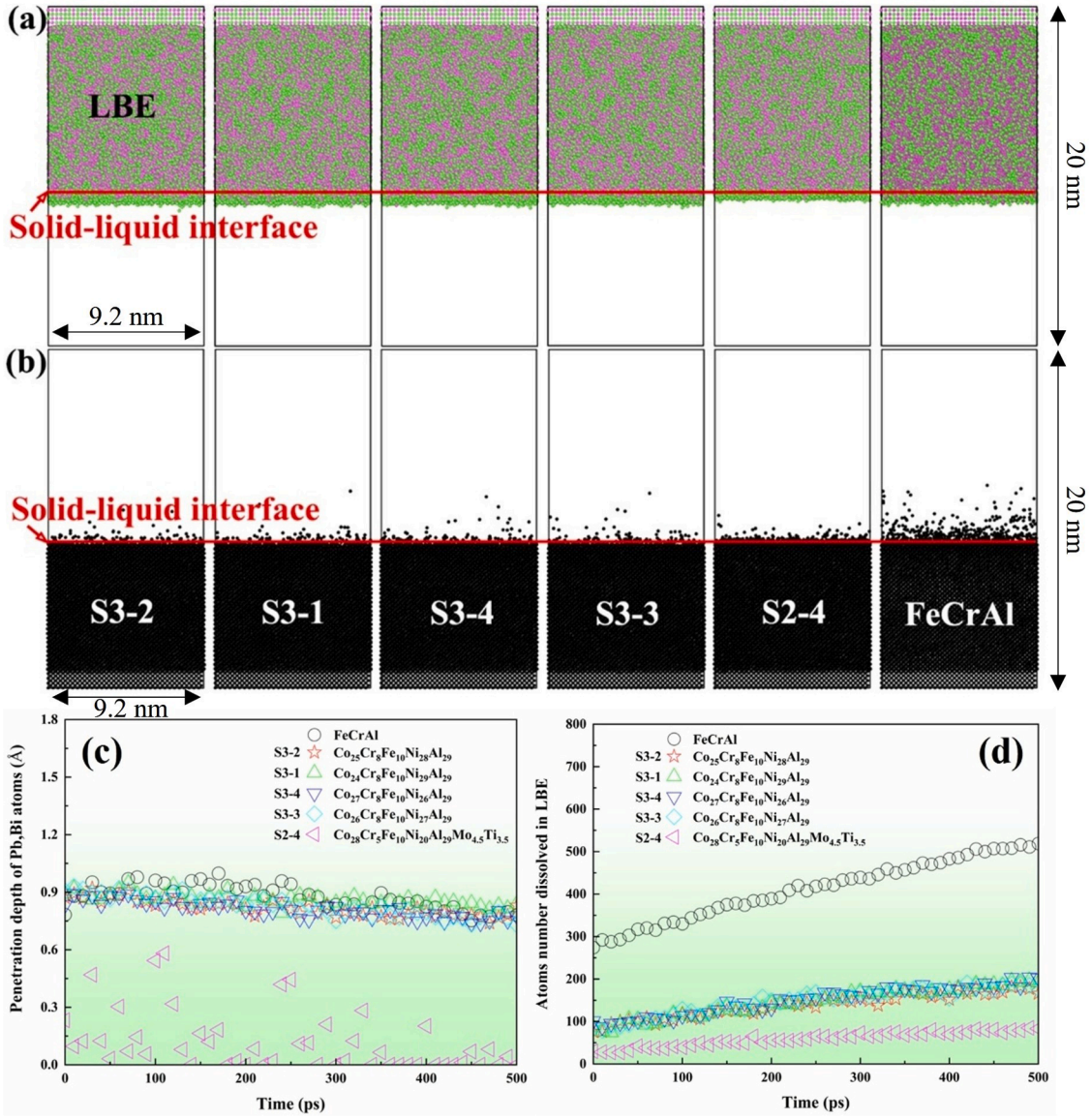

Fig. 9. Performance assessment of material samples obtained from the search in Process II: (a) liquid LBE alloy penetration; (b) matrix atom dissolution; (c) depth of liquid LBE penetration into the matrix; (d) number of matrix atoms dissolved in liquid LBE.

1.33 MeV [58]. The presence of Co-60 creates significant challenges for radioactive waste management, personnel exposure during maintenance operations, and long-term repository storage. Consequently, nuclear-grade structural materials typically specify Co content below 0.05–0.2 wt% depending on the specific application and neutron flux environment. For fusion reactor materials, such as those specified for ITER, Co is classified as a high-activation element requiring strict minimization [59]. Mo contributes to induced radioactivity through the formation of Mo-99 via neutron capture, which has a half-life of 66 h [58]. Although considerably shorter-lived than Co-60, Mo-99 contributes to short-term radioactivity concerns during reactor operation and maintenance outages. Low-activation structural materials for fusion applications generally impose limitations on Mo content as well. The Co and Mo contents in the optimized alloys substantially exceed typical nuclear-grade specifications for structural components in neutron flux environments, and these compositions are therefore not directly applicable to nuclear reactor systems without further compositional modification.

In addition to Co and Mo, the RF importance analysis identified Al as the most influential element for LBE penetration resistance, followed by Fe and Cr. The dominant role of Al is consistent with the well-established protective mechanism of Al_2O_3 layer formation observed in FeCrAl alloys exposed to LBE environments [9,10,60–62]. Fe ranks second due to its high dissolution tendency in LBE, and reducing Fe content directly improves corrosion resistance. The preferential dissolution of Fe over other alloying elements has been confirmed both by our previous MD study [36] and by experimental observations in steel-LBE systems [63]. The significant contribution of Cr can be attributed to its role in forming a Cr_2O_3 sublayer that provides supplementary protection beneath the Al_2O_3 layer [9,10]. The agreement between the RF-derived element importance ranking and these established corrosion mechanisms validates the reliability of the present computational screening approach. It should be acknowledged that MD simulations and experimental corrosion tests differ by 6–9 orders of magnitude in timescale. MD simulations capture initial atomic-scale dissolution processes at picosecond timescales, whereas experiments reflect cumulative corrosion effects over hours to thousands of hours. However, since all simulations in this study were conducted under identical conditions, the relative performance ranking among different compositions provides a reliable basis for preliminary screening.

Table 3
Compositions of nuclear-compatible alloys evaluated by MD simulations (at.%).

Alloy	Al	Cr	Fe	Ni	Mo	Description
NC-1	25	20	30	25	0	Co-free HEA, high Al
NC-2	20	25	30	25	0	Co-free HEA, high Cr
NM-1	20	20	30	25	5	Co-free HEA with Mo
NM-2	15	25	30	26	4	Co-free HEA with Mo
REF-1	0	18	67	13	2	Mo-containing austenitic stainless steel
REF-2	0	20	70	10	0	Conventional austenitic stainless steel

To provide guidance for nuclear applications with stringent elemental restrictions, supplementary MD simulations were performed to evaluate the LBE corrosion resistance of Co-free alloy compositions. The simulations were constrained to the Cr-Fe-Ni-Al-Mo system due to interatomic potential availability, and all simulation parameters, including temperature, immersion duration, and model dimensions, were kept identical to those described in Section 2 to ensure direct comparability with the results presented above. The compositions were designed based on the element importance ranking established in this study, supplemented by conventional austenitic stainless steel compositions for comparison [64]. It should be noted that the suitability of any candidate composition for specific nuclear applications ultimately requires detailed activation calculations and safety assessments, which are beyond the scope of the present computational screening study. The simulated compositions are summarized in Table 3.

Fig. 10 presents the simulation results for nuclear-compatible compositions. NC-1 ($Al_{25}Cr_{20}Fe_{30}Ni_{25}$) demonstrates superior performance among all Co-free alloys, exhibiting the lowest penetration depth and dissolution quantity after 500 ps immersion. The Co-free HEAs rank in the order NC-1 > NM-1 > NC-2 > NM-2 with respect to corrosion resistance. Al content appears to be the primary factor controlling this ranking, NC-1 contains 25 at.% Al and shows the best resistance, whereas NM-2 with only 15 at.% Al exhibits the poorest performance. Such compositional trends corroborate the RF importance analysis results identifying Al as the key element for LBE corrosion resistance. An interesting observation is that NM-1 outperforms NC-2 even though both contain 20 at.% Al. The 5 at.% Mo addition in NM-1 likely accounts for this difference, which aligns with our earlier finding that Mo retards LBE penetration [36]. REF-1 exhibits corrosion resistance comparable to FeCrAl, which can be attributed to their similarly high Fe content. Since Fe exhibits the highest dissolution tendency among the principal elements, the high Fe content in both alloys limits their corrosion resistance regardless of other compositional differences. REF-2 demonstrates inferior performance relative to FeCrAl, with penetration depth approximately 20% higher and dissolution quantity approximately 15% greater. This degraded performance reflects the complete absence of both Al and Mo in the REF-2 composition, highlighting the critical importance of Al addition for LBE corrosion resistance. It should be noted that although the Co-free HEAs exhibit improved corrosion resistance compared to FeCrAl and conventional stainless steels, none of them match the performance of the ML-optimized composition S2–4. This performance gap confirms the significant contribution of Co to LBE corrosion resistance, as Co exhibits the lowest dissolution tendency among the principal elements. For nuclear applications where Co must be restricted, the Co-free HEAs represent a viable compromise that trades some corrosion resistance for compliance with activation constraints, and further optimization within the Co-free compositional space warrants investigation.

6. Conclusions

This study presents an integrated machine learning–molecular dynamics framework to accelerate the computational discovery of materials with improved resistance to corrosion in liquid lead–bismuth eutectic (LBE). The methodology explores extensive compositional spaces (3 million to 400 million samples in the Co–Cr–Fe–Ni–Al–Mo–Ti system) through multi-round iterative optimization. Within the present MD conditions, the optimized $Co_{28}Cr_5Fe_{10}Ni_{20}Al_{29}Mo_{4.5}Ti_{3.5}$ composition exhibits a simulated LBE penetration depth and dissolution quantity both reduced to roughly one-eighth of those of nuclear-grade FeCrAl under identical conditions. Given the nanometer length scale and subnanosecond time scale of MD, these metrics are intended for comparative screening and ranking rather than direct prediction of long-term corrosion rates or reactor lifetimes. The composition window was intentionally broadened for mechanistic interrogation and ML model training; therefore, the predicted compositions should be regarded as computational screening outcomes rather than deployment recommendations. In particular, the high Co and Mo contents in the optimized alloys substantially exceed nuclear-grade specifications, and these compositions are not directly applicable to nuclear reactor systems.

This synergistic integration of machine learning and molecular dynamics can significantly accelerate the materials development cycle by leveraging computationally generated data, particularly for atomic-scale insights that are difficult to obtain experimentally. For nuclear-oriented materials development, the present workflow can be coupled with additional engineering constraints to guide practical down-selection and subsequent experimental validation. Future work will focus on measuring macroscopic dissolution rates, assessing oxide layer stability, and characterizing corrosion products in the LBE environment to support and refine the computational predictions proposed in this paper. The successful application of ML–MD integration establishes a robust paradigm for accelerating material discovery, demonstrating its

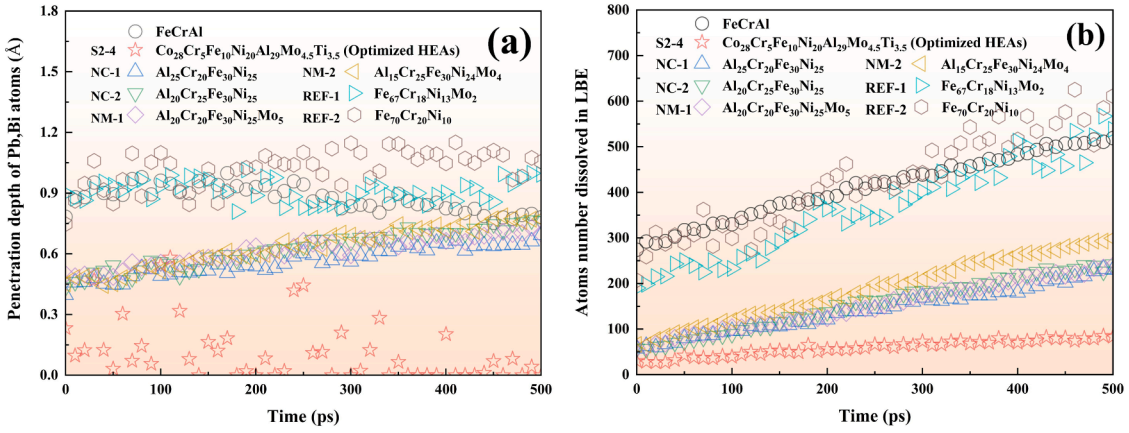

Fig. 10. Performance assessment of material samples with different alloy compositions: (a) depth of liquid LBE penetration into the matrix; (b) number of matrix atoms dissolved in liquid LBE.

potential for broader application to other corrosion-resistant material systems.

CRediT authorship contribution statement

Weihan Li: Writing – review & editing, Writing – original draft, Supervision, Resources, Project administration, Methodology, Funding acquisition, Conceptualization. **Wenrui Wang:** Writing – review & editing, Writing – original draft, Validation, Methodology, Funding acquisition, Formal analysis, Data curation. **Qing Peng:** Writing – review & editing, Writing – original draft, Resources, Methodology, Investigation, Funding acquisition. **Lu Xie:** Methodology, Investigation, Data curation.

Declaration of competing interest

The authors declare that they have no known competing financial interests or personal relationships that could have appeared to influence the work reported in this paper.

Acknowledgement

The authors would like to gratefully acknowledge the National Science and Technology Major Project (Grant No J2020-V-0004–0030). Q. P. would like to acknowledge the support provided by National Natural Science Foundation of China (Grant No 12272378).

Supplementary materials

Supplementary material associated with this article can be found, in the online version, at doi:10.1016/j.jnucmat.2026.156607.

Data availability

No data was used for the research described in the article.

References

[1] Alemberti, The lead fast reactor: an opportunity for the future, Engineering 2 (2016) 59–62, https://doi.org/10.1016/J.ENG.2016.01.022.
[2] L.C. Zhang, Y.F. Zhang, Advancements and development trends in lead-cooled fast reactor core design, Processes 13 (2025) 1773, https://doi.org/10.3390/pr13061773.
[3] X.Y. Zhang, C. Li, Y.X. Wang, M. Huang, Research progress on liquid metal corrosion behavior of structural steels for lead fast reactor, J. Chin. Soc. Corros. Prot. 43 (2023) 1216–1224, https://doi.org/10.11902/1005.4537.2022.338.
[4] Z.F. Ye, P. Wang, H. Dong, D.Z. Li, Oxidation mechanism of T91 steel in liquid lead-bismuth eutectic: with consideration of internal oxidation, Sci. Rep. 6 (2016) 35268, https://doi.org/10.1038/srep35268.
[5] F. Gnecco, E. Ricci, C. Bottino, Corrosion behaviour of steels in lead-bismuth at 823 K, J. Nucl. Mater. 335 (2004) 185–188, https://doi.org/10.1016/j.jnucmat.2004.07.013.
[6] S.W. Feng, H.L. Dai, X.Y. Sun, K.J. Jiang, New insight of the enhanced oxidation resistance of T91 steel in 450 °C liquid lead-bismuth eutectic by adding Al and Si element, J. Mater. Sci. Technol. 204 (2025) 29–46, https://doi.org/10.1016/j.jmst.2024.03.033.
[7] W.T. Wang, C.X. Yang, Y.H. You, H.W. Yin, A review of corrosion behavior of structural steel in liquid lead-bismuth eutectic, Crystals 13 (2023) 968, https://doi.org/10.3390/cryst13060968.
[8] X.X. Wei, B. Zhang, B. Wu, Y.J. Wang, Enhanced corrosion resistance by engineering crystallography on metals, Nat. Commun. 13 (2022) 726, https://doi.org/10.1038/s41467-022-28368-8.
[9] W. Zhang, M.Y. Zhou, J.G. Deng, Y.L. Zhong, Improved LBE corrosion resistance of the FeCrAl coating by the addition of trace Si element, Intermetallics 166 (2024) 108197, https://doi.org/10.1016/j.intermet.2024.108197.
[10] L.Y. Ma, P.F. Tai, Z.G. Wang, L.L. Pang, Research progress on liquid LBE/Pb corrosion of FeCrAl alloys, Mater. Rev. 36 (2022) 195–200, https://doi.org/10.11896/cldb.20100178.
[11] S.J. Liu, C. Yang, Machine learning design for high-entropy alloys: models and algorithms, Metals 14 (2024) 235, https://doi.org/10.3390/met14020235.
[12] X. Gong, H.T. Chen, F.F. Zhang, W.J. Zhu, Degradation of tensile mechanical properties of two Al_xCoCrFeNi (x=0.3 and 0.4) high-entropy alloys exposed to liquid lead-bismuth eutectic at 350 and 500 °C, J. Nucl. Mater. 558 (2022) 153364, https://doi.org/10.1016/j.jnucmat.2021.153364.
[13] J.G. Deng, J. Yang, L.L. Lv, W. Zhang, Q.S. Chen, Corrosion behavior of refractory TiNbZrMoV high-entropy alloy coating in static lead-bismuth eutectic alloy: a novel design strategy of LBE corrosion-resistant coating, Surf. Coat. Tech. 448 (2022) 128884, https://doi.org/10.1016/j.surfcoat.2022.128884.
[14] L.R. Cao, C.Y. Zhang, D.L. Zhang, Recent developments in using molecular dynamics simulation techniques to study biomolecules, Acta Phys.-Chim. Sin. 33 (2017) 1354–1365, https://doi.org/10.3866/PKU.WHXB201704144.
[15] Z.H. Sun, J. Zhang, X.X. Gao, L. Xie, C.Y. Li, Tensile mechanical properties of CoCrFeNiTiAl high entropy alloy via molecular dynamics simulations, Intermetallics 142 (2022) 107444, https://doi.org/10.1016/j.intermet.2021.107444.
[16] L. Xie, G.D. Wu, Q. Peng, J.P. Liu, D.Y. Li, W.R. Wang, An atomistic study on grain-size and temperature effects on mechanical properties of polycrystal CoCrFeNi high-entropy alloys, Mater. Today Commun. 37 (2023) 107264, https://doi.org/10.1016/j.mtcomm.2023.107264.
[17] J. Xiong, P. Deng, E. Jiang, B. Gong, Research progress on microscale simulation of interaction between liquid lead-bismuth eutectic and steel materials, Corros. Pro. 44 (2023) 41–45, https://doi.org/10.11973/fsyfh-202305008.
[18] Maulana, Z. Su'ud, K.D. Hermawan, Khairurrijal, Simulation study of steels corrosion phenomenon in liquid lead-bismuth cooled reactors using molecular dynamics methods, Prog. Nucl. Energ. 50 (2008) 616–620, https://doi.org/10.1016/j.pnucene.2007.11.087.
[19] Y. Gao, G. Raos, C. Cavallotti, Molecular dynamics simulation on physical properties of liquid lead, bismuth and lead-bismuth eutectic (LBE), Pro. Eng. 157 (2016) 214–221, https://doi.org/10.1016/j.proeng.2016.08.359.
[20] Y. Gao, M. Takahashi, C. Cavallott, Molecular dynamics simulation of metallic impurity diffusion in liquid lead-bismuth eutectic (LBE), J. Nucl. Mater. 501 (2018) 253–260, https://doi.org/10.1016/j.jnucmat.2018.01.044.
[21] T. Zhou, X. Gao, Z.W. Ma, H.L. Chang, T.L. Shen, Atomistic simulation of α-Fe (100)-lead-bismuth eutectic (LBE) solid-liquid interface, J. Nucl. Mater. 555 (2021) 153107, https://doi.org/10.1016/j.jnucmat.2021.153107.
[22] Arkundato, Z. Su'ud, M. Abdullah, Corrosion study of Fe in a stagnant liquid Pb by molecular dynamics methods, AIP Con. Pro. 1244 (2010) 136–144, https://doi.org/10.1063/1.3462751.
[23] Z. Arkundato, M. Su'ud, W. Abdullah, Numerical study: iron corrosion-resistance in lead-bismuth eutectic coolant by molecular dynamics method, AIP Con. Pro. 1448 (2012) 155–163, https://doi.org/10.1063/1.4725450.
[24] J. Liu, C.J. Zhao, W.Q. Lu, Molecular dynamics simulation on the corrosion characteristics of iron in liquid lead, Ann. Nucl. Energy 116 (2018) 31–41, https://doi.org/10.1016/j.anucene.2018.02.025.
[25] L.M. Chen, S. Xu, X.X. He, Q.L. Cao, Molecular dynamics study of corrosion behavior of iron with vacancies exposed to lead-bismuth eutectic, Mater. Corros. 74 (2023) 793–802, https://doi.org/10.1002/maco.202213375.
[26] J.T. Xue, J.T. Huang, Z.H. Lai, N. Qu, Machine learning-accelerated prediction of mechanical and microstructural properties of BCC Fe-Cr-Ni-Al high-entropy alloys across the full compositional space, Intermetallics 183 (2025) 108827, https://doi.org/10.1016/j.intermet.2025.108827.
[27] S. Swateelagna, M. Singh, M.R. Rahul, Explainable machine learning based approach for the design of new refractory high entropy alloys, Intermetallics 167 (2024) 108198, https://doi.org/10.1016/j.intermet.2024.108198.
[28] C.Z. Fu, C.C. Tao, H.J. Huang, G. Zhou, Exploring microstructure evolution and machine-learning methods based on SCAT-CIWOA-BP-DMM theory during hot deformation of 56Ni-32Ti-12Hf alloy, Intermetallics 171 (2024) 108342, https://doi.org/10.1016/j.intermet.2024.108342.
[29] E. Halpren, X. Yao, Z.W. Chen, Machine learning assisted design of BCC high entropy alloys for room temperature hydrogen storage, Acta Mater. 270 (2024) 119841, https://doi.org/10.1016/j.actamat.2024.119841.
[30] N.S. Klimenko, R. Ryltsev, N. Yurchenko, Machine learning assisted design of new ductile high-entropy alloys: application to Al-Cr-Nb-Ti-V-Zr system, Intermetallics 175 (2024) 108469, https://doi.org/10.1016/j.intermet.2024.108469.
[31] L. Chen, A. Jarlöv, H.L. Seet, Y.F. Li, Exploration of V-Cr-Fe-Co-Ni high-entropy alloys with high yield strength: a combination of machine learning and molecular dynamics simulation, Comp. Mater. Sci. 217 (2023) 111888, https://doi.org/10.1016/j.commatsci.2022.111888.
[32] L. Shen, L. Chen, J.H. Huang, J.C. He, Z.J. Li, Predicting phases and hardness of high entropy alloys based on machine learning, Intermetallics 162 (2023) 108030, https://doi.org/10.1016/j.intermet.2023.108030.
[33] A.P. Thompson, H.M. Aktulga, et al., LAMMPS - a flexible simulation tool for particle-based materials modeling at the atomic, meso, and continuum scales, Comput. Phys. Commun. 271 (2022) 108171, https://doi.org/10.1016/j.cpc.2021.108171.
[34] M.S. Daw, M.I. Baskes, Embedded-atom method: derivation and application to impurities, surfaces, and other defects in metals, Phys. Rev. B 29 (1984) 6443–6453, https://doi.org/10.1103/PhysRevB.29.6443.
[35] L. Xie, G.D. Wu, P.K. Liaw, W.R. Wang, D.Y. Li, Temperature gradient enhances the solidification process and properties of a CoCrFeNi high-entropy alloy: atomic insights from molecular dynamics simulations, Comp. Mater. Sci. 231 (2024) 112538, https://doi.org/10.1016/j.commatsci.2023.112538.
[36] W.R. Wang, W.H. Li, L. Xie, Effects of temperature and trace elements on the mechanical properties and dissolution-diffusion characteristics of CoCrFeNi in liquid LBE: atomic insights from molecular dynamics, J. Nucl. Mater. 613 (2025) 155861, https://doi.org/10.1016/j.jnucmat.2025.155861.
[37] L. Xie, G.D. Wu, Q. Peng, W.R. Wang, Molecular dynamics simulation on the dissolution and diffusion characteristics of FeCrAl alloy in liquid LBE, Ann. Nucl. Energy 192 (2023) 109983, https://doi.org/10.1016/j.anucene.2023.109983.

[38] K. Belashchenko, Computer simulation of the properties of liquid metals: gallium, lead, and bismuth, Russ. J. Phys. Chem. A 86 (2012) 779–790, https://doi.org/10.1134/S0036024412050056.
[39] G. Benamati, C. Fazio, H. Piankova, A. Rusanov, Temperature effect on the corrosion mechanism of austenitic and martensitic steels in lead-bismuth, J. Nucl. Mater. 301 (2002) 23–27, https://doi.org/10.1016/S0022-3115(01)00723-1.
[40] J. Yang, F.F. Zhang, L.H. Zhai, Microstructure, mechanical and oxygen-deficient lead-bismuth eutectic corrosion properties of FeCrAlTiMo high-entropy alloy coatings for fuel claddings, Intermetallics 175 (2024) 108533, https://doi.org/10.1016/j.intermet.2024.108533.
[41] J. Yang, M.Y. Zhou, L.L. Lv, Y. Zhou, Q. Li, Influence of Si addition on the microstructure, mechanical and lead-bismuth eutectic corrosion properties of an amorphous AlCrFeMoTiSi$_x$ high-entropy alloy coating, Intermetallics 148 (2022) 107649, https://doi.org/10.1016/j.intermet.2022.107649.
[42] W.Y. Li, J. Zhou, J. Zhang, H. Ren, Corrosion behavior and mechanisms of rare-earth ferrite/martensite steel weldment in liquid lead-bismuth eutectic, Corros. Sci. 249 (2025) 112840, https://doi.org/10.1016/j.corsci.2025.112840.
[43] G.J. Zhu, J. Tan, Z.Q. Xing, J.Y. Pang, Effect of Ti addition on corrosion behaviors of Fe-Ni-Cr-Al high entropy alloys exposed to static lead-bismuth eutectic at 550°C, Corros. Sci. 236 (2024) 112286, https://doi.org/10.1016/j.corsci.2024.112286.
[44] X.L. Wang, Y.C. Jin, S. Schmitt, Recent advances in bayesian optimization, ACM. Comput. Surv. 55 (2023) 1–36, https://doi.org/10.1145/3582078.
[45] B.V. Khatamsaz, P. Singh, D.D. Johnson, D. Allaire, Multi-objective materials bayesian optimization with active learning of design constraints: design of ductile refractory multi-principal-element alloys, Acta Mater. 236 (2022) 118133, https://doi.org/10.1016/j.actamat.2022.118133.
[46] L.Y.M. Chen, Y. Zhang, Accelerating the design of high-entropy alloys with high hardness by machine learning based on particle swarm optimization, Intermetallics 154 (2023) 107819, https://doi.org/10.1016/j.intermet.2022.107819.
[47] S.V. Saraiva, F.D.O. Carvalho, C.A.G. Santos, Daily streamflow forecasting in Sobradinho Reservoir using machine learning models coupled with wavelet transform and bootstrapping, Appl. Soft. Comput. 102 (2021) 107081, https://doi.org/10.1016/j.asoc.2021.107081.
[48] Y.P. Diao, L.C. Yan, K.W. Gao, A strategy assisted machine learning to process multi-objective optimization for improving mechanical properties of carbon steels, J. Mater. Sci. Technol. 109 (2022) 86–93, https://doi.org/10.1016/j.jmst.2021.09.004.
[49] Y.Z. Wen, C.X. Wang, D.Z. Xue, Y. Bai, S. Antonov, Machine learning assisted design of high entropy alloys with desired property, Acta Mater. 170 (2019) 109–117, https://doi.org/10.1016/j.actamat.2019.03.010.
[50] D.C. Montgomery, E.A. Peck, G.G. Vining, Introduction to Linear Regression Analysis, 6th ed., John Wiley & Sons, Hoboken, 2021.
[51] Ostertagová, Modelling using polynomial regression, Proc. Eng. 48 (2012) 500–506, https://doi.org/10.1016/j.proeng.2012.09.545.
[52] A.J. Smola, B. Schölkopf, A tutorial on support vector regression, Stat. Comput. 14 (2004) 199–222, https://doi.org/10.1023/B:STCO.0000035301.49549.88.
[53] W.Y. Loh, Classification and regression trees, WIREs Data Min. Knowl. Discov. 1 (2011) 14–23, https://doi.org/10.1002/widm.8.
[54] J. Li, J.H. Cheng, J.Y. Shi, F. Huang, Brief introduction of back propagation (BP) neural network algorithm and its improvement, in: D. Jin, S. Lin (Eds.), Advances in Computer Science and Information Engineering, Springer, Berlin, 2012, pp. 553–558.
[55] O. Kramer, K-Nearest Neighbors, Dimensionality Reduction With Unsupervised Nearest Neighbors, 1st ed., Springer, Berlin, 2013.
[56] T.L.ë Mezzadri, F. Mathy, Hold-out strategy for selecting learning models: application to categorization subjected to presentation orders, J. Math. Psychol. 109 (2022) 102691, https://doi.org/10.1016/j.jmp.2022.102691.
[57] Y. Qiu, S. Thomas, M.A. Gibson, Corrosion of high entropy alloys, Npj Mat. Degrad. 15 (2017) 1–18, https://doi.org/10.1038/s41529-017-0009-y.
[58] J.K.T. Browne, Nuclear data sheets for A = 60, Nucl. Data Sheets 114 (2013) 1849–2022, https://doi.org/10.1016/j.nds.2013.11.002.
[59] V. Barabash, A. Peacock, S. Fabritsiev, Materials challenges for ITER–Current status and future activities, J. Nucl. Mater. 367-370 (2007) 21–32, https://doi.org/10.1016/j.jnucmat.2007.03.017.
[60] K.A. Terrani, Accident tolerant fuel cladding development: promise, status, and challenges, J. Nucl. Mater. 501 (2018) 13–30, https://doi.org/10.1016/j.jnucmat.2017.12.043.
[61] Y. Yamamoto, B.A. Pint, K.A. Terrani, Development and property evaluation of nuclear grade wrought FeCrAl fuel cladding for light water reactors, J. Nucl. Mater. 467 (2015) 703–716, https://doi.org/10.1016/j.jnucmat.2015.10.019.
[62] B.A. Pint, K.A. Terrani, M.P. Brady, High temperature oxidation of fuel cladding candidate materials in steam–hydrogen environments, J. Nucl. Mater. 440 (2013) 420–427, https://doi.org/10.1016/j.jnucmat.2013.05.047.
[63] J.S. Zhang, A review of steel corrosion by liquid lead and lead–bismuth, Corros. Sci. 51 (2009) 1207–1227, https://doi.org/10.1016/j.corsci.2009.03.013.
[64] S.J. Zinkle, J.T. Busby, Structural materials for fission & fusion energy, Mater. Today 12 (2009) 12–19, https://doi.org/10.1016/S1369-7021(09)70294-9.